



Optical response and band structure of LiCoO₂ including electron-hole interaction effectsSantosh Kumar Radha  and Walter R. L. Lambrecht ^{*}*Department of Physics, Case Western Reserve University, 10900 Euclid Avenue, Cleveland, Ohio 44106-7079, USA*Brian Cunningham  and Myrta Grüning [†]*School of Mathematics and Physics, Queen's University Belfast, Belfast BT7 1NN, Northern Ireland, United Kingdom*Dimitar Pashov  and Mark van Schilfgaarde [‡]*Department of Physics, King's College London, London WC2R 2LS, United Kingdom*

(Received 21 June 2021; accepted 19 August 2021; published 9 September 2021)

The optical response functions and band structures of LiCoO₂ are studied at different levels of approximation, from density functional theory (DFT) in the generalized gradient approximation (GGA) to quasiparticle self-consistent QSGW (with G for Green's function and W for screened Coulomb interaction) without and with ladder diagrams (QSGW \hat{W}) and the Bethe Salpeter Equation (BSE) approach. The QSGW method is found to strongly overestimate the band gap and electron-hole or excitonic effects are found to be important. They lower the quasiparticle gap by only about 11% but the lowest energy peaks in absorption are found to be excitonic in nature. The contributions from different band to band transitions and the relation of excitons to band-to-band transitions are analyzed. The excitons are found to be strongly localized. A comparison to experimental data is presented.

DOI: [10.1103/PhysRevB.104.115120](https://doi.org/10.1103/PhysRevB.104.115120)**I. INTRODUCTION**

LiCoO₂ is a well known material utilized in Li-ion batteries [1–3]. In spite of the extensive literature on this material, its fundamental electronic structure and optical properties are not yet fully understood. Qualitatively, its electronic structure is understood to be a normal band insulator with a low spin configuration in terms of the d -band filling [4,5]. The structure with $R\bar{3}m$ space group consists of layers of edge-sharing CoO₆ octahedra with a triangular Co lattice, with intercalated Li. One may also view it as a layered ordered arrangement of Li and Co ions in a close packed oxygen lattice with both Li and Co octahedrally coordinated. In contrast, another form of LiCoO₂ with disordered spinel structure has both octahedral and tetrahedrally coordinated cations. In the $R\bar{3}m$ structure, the Li donates its electron to the Co-O layer, thus leading nominally to a Co³⁺ ion with d^6 configuration in which the lower Co- d t_{2g} orbital derived bands are filled and the e_g bands are empty [6]. Much attention has been paid to the effects of delithiation and ordering of Li vacancies in Li _{x} CoO₂ [2,3,7,8], including the $x = 0$ end member CoO₂ [9].

However, a quantitative understanding of optical absorption in relation to the band structure is missing. On the experimental side, a lot of confusion seems to arise from the variations in Li content in Li _{x} CoO₂ and dependence on growth

methods, temperature dependent variations in the structure of LiCoO₂, and the deviations from single crystal behavior. Different methods of determining the optical absorption, such as Tauc plots vs reflection or transmission measurements also tend to give different results. On the theory side, band structures in the local density approximation [4,6] of density functional theory seemed to give qualitative agreement with the optical absorption onset near 1.5 eV but, as is a main focus of this paper, the higher accuracy GW many-body-theory results give a much higher gap. A detailed comparison of our calculations with specific measurements is postponed till Sec. III F. The previous theory assignments of the optical features were based only on peak positions but not on actual calculations of the optical response.

In this paper we calculate and analyze the optical response functions based on band structure calculations at different levels of theory. We start by comparing density functional calculations in the generalized gradient approximation (GGA) to quasiparticle self-consistent GW calculations. Next, we calculate the imaginary part of the dielectric function $\epsilon_2(\omega)$ first in the long-wavelength approximation from a summation over the interband transitions and analyze the contributions from different bands to the main peaks based on the QSGW bands. We then calculate $\epsilon_2(\omega)$ including local field effects in the random phase approximation (RPA) and using the Bethe-Salpeter equation (BSE) method including thereby electron-hole interaction effects. The electron-hole interaction effects or ladder diagrams in the calculation of W , the screened Coulomb interaction, are also included here at finite wave vector q and we call this band structure the QSGW \hat{W} band structure because it includes vertex (Γ) corrections to W .

^{*}walter.lambrecht@case.edu[†]Also at European Theoretical Spectroscopy Facility (ETSF).[‡]Also at National Renewable Energy Laboratory, Golden, CO 80401, USA

We find that the QSGW band gap is significantly higher (~ 4 eV) than the GGA gap, which is not unusual, but also larger than the experimental values. While QSGW reduces the Σ correction by about 11%, the gap is still significantly higher than experiment. We show that the lowest peaks in absorption are in fact excitonic in nature and significantly lower the optical gap E_g^{opt} compared to the fundamental one-particle gap, which is defined as the difference between the ionization potential and the electron affinity $E_g^{(qp)} = I - A$. The electron affinity is defined as the lowest energy for adding an electron [$A = E(N) - E(N + 1)$] and the ionization potential as the energy for extracting an electron [$I = E(N - 1) - E(N)$].

II. COMPUTATIONAL METHODS

All the calculations done here make use of the full-potential linearized muffin-tin orbital method (FP-LMTO) [12,13] as implemented in the Questaal package [14,15]. This is an all-electron method without shape approximations to the potentials. In the density functional calculations we use the generalized gradient approximation (GGA) in the Perdew-Burke-Ernzerhof (PBE) [16] parametrization. The quasiparticle self-consistent GW method (QSGW) is described in Ref. [17]. It is based on Hedin's many-body-perturbation theoretical method in which the dynamical self-energy is given schematically as $\Sigma(\omega) = G(\omega) \otimes W(\omega')$ with \otimes meaning convolution in energy and \mathbf{k} space. Here $G(\omega)$ is the one-particle Green's function corresponding to the starting independent particle H^0 Hamiltonian [usually the local density approximation (LDA) or GGA at first], and $W(\omega)$ is the screened Coulomb interaction, $W(\omega) = [1 - vP(\omega)]^{-1}v$ in which v is the bare Coulomb interaction and $P(\omega)$ is the polarization propagator, which can also be obtained from the Green's function G or directly from the eigenvalues ϵ_i and eigenstates $|\psi_i\rangle$ of the H^0 Hamiltonian. Here the index i is shorthand for band number n and \mathbf{k} point in the Brillouin zone. From this self-energy, a nonlocal but energy independent exchange-correlation potential $\tilde{\Sigma}_{ij} = \frac{1}{2}\text{Re}\{\Sigma_{ij}(\epsilon_i) + \Sigma_{ij}(\epsilon_j)\}$ is extracted in the basis of the eigenstates of the H^0 Hamiltonian. This new exchange-correlation potential now replaces the one in H^0 and the procedure is iterated till convergence, at which point the eigenvalues ϵ_i of H^0 become identical to the quasiparticle energies E_i which have the meaning of one-electron extraction and addition energies to the many-electron system.

Note that in the above procedure the RPA is usually used in calculating W . This tends to underestimate the screening. A significant improvement consists of including electron-hole interactions or ladder diagrams in the calculation of W via the BSE as described by Cunningham *et al.* [18,19]. We will denote this new W by \hat{W} . Please note that it plays a similar role to \hat{W} in other approaches which use a time-dependent DFT kernel f_{xc} to correct W [20–22]. Our approach is equivalent to including a specific approximation for the vertex in the calculation of P in the context of the Hedin equations, namely $\delta\Sigma(12)/\delta G(34) = iW(12)\delta(13)\delta(24)$ is evaluated from $\Sigma = iGW$ assuming that $\delta W/\delta G \approx 0$. Here the numbers represent real space, spin, and time variables $1 \equiv (\mathbf{r}_1, \sigma_1, t_1)$. The vertex

then becomes

$$\Gamma(123) = \delta(12)\delta(13) + i \int d(67)W(12)G(16)G(72)\Gamma(673) \quad (1)$$

and introducing the four-point $P^{\text{RPA}}(1234) = -iG(13)G(42)$ allows us to cast this in terms of a BSE approach, in which $P(12) = P(1122)$ is obtained from

$$P(12) = P_{\text{RPA}}(12) - \int P_{\text{RPA}}(1134)W(34; \omega = 0)P(3422)d(34). \quad (2)$$

As usual, we here make a static approximation for W for the inclusion of the electron-hole effects. This has mainly been validated by its success in describing optical response. Going beyond it would significantly increase the complexity of the method [23]. Marini and Del Sole [23] showed that including the exciton dynamics partially undoes the renormalization effects of the quasiparticle self-energy. However, this may be different in our QSGW approach which relies on error cancellations of such renormalization effects.

At present we do not include a corresponding vertex correction in the calculation of the self-energy. Grüneis *et al.* [24] found first-order vertex corrections in the self-energy to improve mainly the absolute ionization potentials while only moderately affecting band gaps for various weakly correlated semiconductors. For small molecules, Maggio *et al.* [25] found that when applying $G_0W_0\Gamma$ to a Hartree-Fock starting point, including the vertex in W , improved ionization potentials while including the vertex also for the self-energy worsened results. While vertex corrections in Σ were found to be important in the context of self-consistent implementation of the Hedin equations by Kutepov [26,27], our quasiparticle self-consistent approach has a different aim, namely to provide the best one-particle starting point for G and the best possible screening in W to provide accurate quasiparticle energies within the GW approximation. As we showed in our introduction of the QSGW approximation, quasiparticleization of G greatly reduces errors introduced by omitting Γ in Σ (see Appendix A, Ref. [17]). Calling G^0 the quasiparticle G , we can write $G = ZG^0 + \tilde{G}$, where \tilde{G} is the incoherent part. On the other hand, in the $\omega \rightarrow 0$, $\mathbf{q} \rightarrow 0$ limit there is a Ward identity $\Gamma \rightarrow 1/Z$. This Z factor approximately cancels the one in GW with the replacement $G \rightarrow G^0$. While it would be of interest to study the effect of vertex corrections in $\Sigma = iGW\Gamma$, as the equations are somewhat imbalanced by including only the vertex in W , it is beyond the scope of the present paper.

The optical response is given in terms of the macroscopic dielectric function, in particular its imaginary part $\epsilon_2(\omega)$, from which the real part $\epsilon_1(\omega)$ can be obtained by Kramers-Kronig transformation and from it all other relevant optical functions, such as the complex index of refraction, absorption coefficient, and reflectivity. A first way to calculate this is through the Adler-Wiser equation in the independent particle, long-wavelength limit

$$\epsilon_2(\omega) = \frac{8\pi^2 e^2}{\Omega\omega^2} \sum_n \sum_{n'} \sum_{\mathbf{k} \in \text{BZ}} f_{n\mathbf{k}}(1 - f_{n'\mathbf{k}}) |\langle \psi_{n\mathbf{k}} | [H, \mathbf{r}] | \psi_{n'\mathbf{k}} \rangle|^2 \delta(\omega - \epsilon_{n'\mathbf{k}} + \epsilon_{n\mathbf{k}}). \quad (3)$$

The optical matrix elements here are the velocity matrix elements $\hat{\mathbf{r}} = (i/\hbar)[H, \mathbf{r}]$, which for a local potential can be written in terms of the momentum matrix elements $\mathbf{v} = \mathbf{p}/m$. So, when using the LDA or GGA band structure and eigenstates, this is correct but when using the *GW* band structure as input, one needs to renormalize the matrix elements. One way to do this, proposed by Levine and Allan [28] in the context of a scissor-operator corrections, consists of rescaling the matrix elements by a factor $(\epsilon_{n\mathbf{k}} - \epsilon_{n\mathbf{k}}^{\text{LDA}})/(\epsilon_{n\mathbf{k}}^{\text{LDA}} - \epsilon_{n\mathbf{k}}^{\text{LDA}})$. Alternatively, $d\tilde{\Sigma}/dk$ terms need to be explicitly included. We follow the latter.

A second, more accurate formulation is to calculate

$$\epsilon_M(\omega) = \lim_{\mathbf{q} \rightarrow 0} \frac{1}{\epsilon_{\mathbf{G}=0, \mathbf{G}'=0}^{-1}(\mathbf{q}, \omega)} \quad (4)$$

in a basis set of plane waves. This formulation includes local-field effects, whereas the above Adler-Wiser equation does not. Within this formulation one may now either approximate $\epsilon_{\mathbf{G}, \mathbf{G}'}^{-1}(\mathbf{q}, \omega)$ by including the Coulomb interaction in $\epsilon^{-1} = (1 - vP)^{-1}$, but neglecting electron-hole interactions [carried by W in Eq. (6)] called the RPA, or by using the BSE including electron-hole interactions as described in Cunningham *et al.* [18]. This step is formulated in terms of four-particle polarization operators and more specifically, one calculates the modified response function [29,30]

$$\begin{aligned} \bar{P}(1234) &= P^0(1234) \\ &+ \int d(5678) P^0(1256) K(5678) \bar{P}(7834) \end{aligned} \quad (5)$$

with the kernel

$$K(1234) = \delta(12)(34)\bar{v} - \delta(13)\delta(24)W(12). \quad (6)$$

Again, we may also here replace W by \hat{W} for an even better approximation and we use a static approximation $W(\omega = 0)$ in solving the BSE equation (5) [19]. Finally, note that $\bar{v}_{\mathbf{G}}(\mathbf{q}) = 4\pi/|\mathbf{q} + \mathbf{G}|^2$ if $\mathbf{G} \neq 0$ and zero otherwise. The macroscopic dielectric function is then given by

$$\epsilon_M(\omega) = 1 - \lim_{\mathbf{q} \rightarrow 0} v_{\mathbf{G}=0}(\mathbf{q}) \bar{P}_{\mathbf{G}=\mathbf{G}'=0}(\mathbf{q}, \omega). \quad (7)$$

Essentially, this approach amounts to analytically finding the relevant matrix element $\mathbf{G} = \mathbf{G}' = 0$ of the inverse of the dielectric matrix by a block matrix inversion approach as explained in Appendix B of Ref. [30]. In practice the Dyson equation for \bar{P} is solved in the basis set of single-particle eigenfunctions as described by Cunningham *et al.* [18]. Eventually, the bare and screened Coulomb matrices in the kernel are first written in terms of the mixed product basis set ($|M_J^q\rangle$) used also in the *GW* implementation and then converted to the single-particle basis set to derive an effective two-particle Hamiltonian which is then diagonalized to obtain the final forms of the macroscopic dielectric function $\epsilon_M(\omega)$ including the optical matrix elements (see Eqs. (23)–(25) in Ref. [18]). The optical matrix elements of the velocity operator are obtained including the momentum derivative of the self-energy [18]. The use of the mixed product/interstitial plane wave auxiliary basis was designed to represent the polarization P more efficiently than is possible with traditional plane wave basis sets. In the latter case the polarizability is obtained by the Adler-Wiser construction, which involves terms of a sum over

all empty eigenstates. It is in principle exact for the RPA polarizability, but it is known to converge slowly and alternative schemes have been proposed [31–33]. The situation is quite different for the basis we use: quasiparticle levels converge very quickly with the rank of the basis set, as was shown in some detail for a number of semiconductors [34]. This rapid convergence is slightly misleading, however, because in the augmentation region the basis set does not change except with the addition of local orbitals. Our present scheme allows the use of one local orbital per l channel, but it has been shown [35] that for full convergence, either more than one is required or that the partial waves are generalized to be frequency dependent [33]. This error is fairly small: in the case of ZnO, which is a worst case scenario, the discrepancy between a fully converged result [36] and the present method in the G_0W_0 approximation [34] is approximately 0.2 eV. High-energy local orbitals were also shown to be important in Ref. [37].

Adding ladder diagrams in the calculation of W proceeds similarly by solving the Dyson-like Eq. (2) [19]. This is done in the “transition space” by expanding the four-point quantities in one-particle eigenfunctions. We then solve a BSE equation for the two-particle Hamiltonian:

$$\begin{aligned} H_{n_1 n_2 n_3 n_4} &= (\epsilon_{n_2} - \epsilon_{n_1}) \delta_{n_1, n_3} \delta_{n_2, n_4} \\ &+ (f_{n_4} - f_{n_3}) W_{n_1 n_2 n_3 n_4}(\omega = 0), \end{aligned} \quad (8)$$

where f_n are Fermi functions. We work within the Tamm-Dankoff approximation (TDA), and using a static $W(\omega = 0)$, which means that $n_1 = v$, $n_2 = c$, $n_3 = v'$, $n_4 = c'$ are restricted to be valence and conduction band states. The TDA has been found to be adequate for calculation of optical absorption, in particular when combined with the modified response function approach by Hanke [29] as shown by explicitly going beyond it in Ref. [38]. Its validity for finite \mathbf{q} is less well established but going beyond the TDA significantly increases the computational effort by requiring a non-Hermitian and double sized matrix to be inverted. While including here finite q electron-hole interactions, we expect their major effect on the response to occur for the long-wavelength limit. After diagonalizing this two-particle Hamiltonian,

$$H_{vc, v'c'} A_{v', c'}^\lambda = E_\lambda A_{v, c}^\lambda. \quad (9)$$

The four-particle polarization is contracted back to a two-particle one and reexpressed in the mixed-product basis set. We should also keep in mind that each valence and conduction state here are associated with a different \mathbf{k} point in the Brillouin zone. We then obtain

$$\begin{aligned} P_{I, J}(\mathbf{q}, \omega) &= \sum_{v, c, v', c'} \sum_{\mathbf{k}, \mathbf{k}'} \langle M_I^q \psi_{v\mathbf{k}} | \psi_{c\mathbf{k}+\mathbf{q}} \rangle \\ &\times \sum_{\lambda} \frac{A_{v\mathbf{k}, c\mathbf{k}+\mathbf{q}}^\lambda [A_{v'\mathbf{k}', c'\mathbf{k}'+\mathbf{q}}^\lambda]^*}{E_\lambda - \omega + i\eta} \\ &\times \langle \psi_{v'\mathbf{k}'} | \psi_{c'\mathbf{k}'+\mathbf{q}} M_J^q \rangle. \end{aligned} \quad (10)$$

Finally, the new W is obtained as

$$\begin{aligned} W_{I, J}(\mathbf{q}, \omega) &= \sqrt{V_I(\mathbf{q})} [1 - \sqrt{V(\mathbf{q})} P(\mathbf{q}, \omega) \sqrt{V(\mathbf{q})}]_{I, J}^{-1} \\ &\times \sqrt{V_J(\mathbf{q})}. \end{aligned} \quad (11)$$

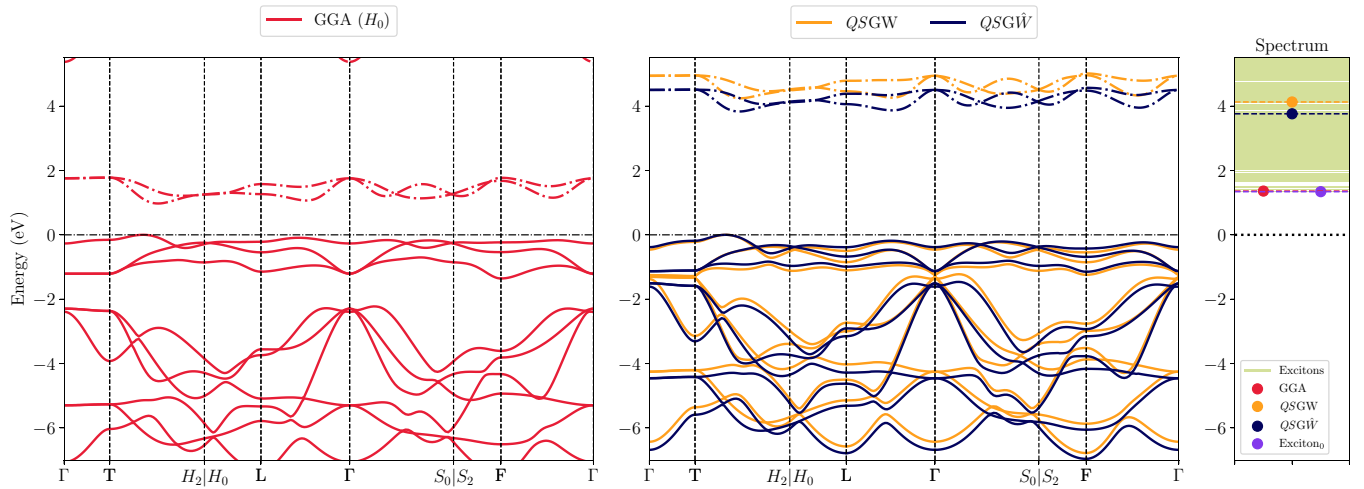


FIG. 1. Band structure of $R\bar{3}m$ LiCoO₂ in GGA (left), and QSGW, QSGW \hat{W} (middle). The Brillouin zone high symmetry point labeling follows Refs. [10,11]. The rightmost figure shows the exciton spectrum of eigenvalues of the two-particle BSE compared with the band gaps at different levels of theory. The \hat{W} is used here for the exciton levels.

We work here in the product basis set which is rotated so that the bare Coulomb interaction is diagonal and its square root can be taken.

We note that obtaining $\hat{W}(\mathbf{q}, \omega)$ requires diagonalizing the two-particle Hamiltonian of the BSE equations for a mesh of \mathbf{q} points and is therefore more demanding than the final form of the macroscopic dielectric function [Eq. (7)] which only requires diagonalizing the two-particle Hamiltonian in the limit $\mathbf{q} \rightarrow 0$. Also using the expression for the macroscopic dielectric function in terms of the modified response function \bar{P} avoids having to invert the full dielectric response matrix.

Calculations are done in the full-potential linearized muffin-tin orbital method. Convergence parameters were chosen as follows: basis set *spdf-sp* spherical wave envelope functions plus augmented plane waves with a cutoff of 3 Ryd, augmentation cutoff $l_{\max} = 4$, \mathbf{k} -point mesh, $12 \times 12 \times 12$. In the *GW* calculations the self-energy Σ is calculated on a \mathbf{k} mesh of $6 \times 6 \times 6$ points and interpolated to the above finer mesh and the bands along symmetry lines using the real space representation of the LMTO basis set.

III. RESULTS

A. Band structure

First, we compare the GGA, QSGW, and QSGW \hat{W} band structures of LiCoO₂ in the $R\bar{3}m$ structure in Fig. 1. The Brillouin zone labeling follows the notation of the Bilbao Crystallography Server [39] which is equivalent to Hinuma *et al.* [11]. The band gap is found to be slightly indirect with VBM and CBM lying between T and H_2 very close to each other but not exactly at the same point. The lowest indirect gap is thus very close to direct gaps at the VBM and CBM or the lowest direct gap. The gaps of interest and \mathbf{k} location of band extrema are summarized in Table I. We can see that the QSGW gap (4.125 eV) is significantly larger than the experimental values mentioned in the Introduction. The GGA gap is somewhat smaller than the reported t_{2g} - e_g gap of about 2 eV and smaller than the value in Czyżyk *et al.* [4] of 1.2 eV. This is related to our use of the GGA lattice constants. We

note that $(E_g^{\text{QSGW}\hat{W}} - E_g^{\text{GGA}})/(E_g^{\text{QSGW}} - E_g^{\text{GGA}}) \approx 0.89$. Thus, adding the ladder diagrams to include the electron-hole effects on the screening of W reduces the gap correction by about 11%, somewhat smaller than the often used ad-hoc 0.8Σ correction factor.

We may also see that the Co- d - t_{2g} bands (between 0 and -2 eV in GGA) have moved closer to the more O- $2p$ like deeper valence bands. We should note that we have used the VBM as reference for both. So, what this really indicates is that the Co- d - t_{2g} bands shift more down by the *GW* self-energy than the O- $2p$, which results from their more localized character. In fact, the top valence band in QSGW \hat{W} shifts down by about 1.33 eV relative to GGA, the conduction band shifts up by about 1.53 eV, and the fourth valence band counting down from the top, which is the top of the O- $2p$ like bands shifts down by only 0.42 eV at Γ .

Finally, we note that convergence of the self-energy with \hat{W} is important. We found that the band gap converges faster to the final result if we apply the ladder diagrams in \hat{W} from the start rather than first doing a QSGW calculation and then adding the ladder diagrams. This is shown in Appendix A.

B. Band to band analysis of optical response

Next, we show the optical response function obtained within the Adler-Wiser form using the QSGW \hat{W} bands and matrix elements in Fig. 2. Along with it, we show the corresponding band structure. The relevant bands are numbered. The vertical axis in the $\epsilon_2(\omega)$ figure is divided into intervals corresponding to specific valence band to conduction bands as numbered in the band figure and the horizontal color bars show their partial contribution to the spectrum on a color scale shown on the right. For example, for $\mathbf{E} \perp \mathbf{c}$ the lowest energy peak, just above 4 eV is almost 100% accounted for by the transition from the top valence band (No. 11) to the lowest conduction band (12) while the peak just above 6 eV is mostly accounted for by bands 8 to 12 transitions. The peak at about 5 eV has a large contribution from bands 10 to 13 transitions. We can also see that there is a significant anisotropy between

TABLE I. Band gaps of $R\bar{3}m$ LiCoO₂ in various approximations and \mathbf{k} location of VBM and VBM.

	GGA	QSGW	QSGW [†]
Smallest indirect gap (eV)	0.867	4.125	3.762
Direct gap at Γ (eV)	2.023	5.401	4.884
\mathbf{k}_{CBM}	(0.612,0.388,0.500)	(0.604,0.396,0.500)	(0.604,0.396,0.500)
\mathbf{k}_{VBM}	(0.604,0.396,0.500)	(0.596,0.404,0.500)	(0.596,0.404,0.500)

the $\mathbf{E} \perp \mathbf{c}$ and $\mathbf{E} \parallel \mathbf{c}$ response. Finally, we note that all peaks up to 10 eV are mainly explained by transitions to the lowest two conduction bands from increasingly deeper valence bands. Transitions from the top of the valence band to higher Co-4s or Li-like band do not appear to make a significant contribution in this range. Details of the higher bands can

be found in Ref. [40] in the GGA. They lie above 6 eV in that case and thus even higher, above 10 eV in QSGW. We therefore do not pay further attention to them here.

C. Local field effects in RPA

Having understood the band-to-band transition relation with the peaks in the optical response, we now turn to the change in the optical response owing to the local field effects. First, we compare the RPA including local field effects with the long-wavelength limit in Fig. 3. In other words, this compares $\lim_{\mathbf{q} \rightarrow 0} \epsilon_{00}(\mathbf{q}, \omega)$ with $\lim_{\mathbf{q} \rightarrow 0} 1/\epsilon_{00}^{-1}(\mathbf{q}, \omega)$. For the in-plane polarization we can see somewhat similar peak structure but there is some tendency of shifting oscillator strength to higher energies and there are also changes in intensity of the peaks. For the out-of-plane polarization, we can see two strong peaks in the RPA result around 6 and 7 eV which are not clearly related to corresponding peaks in the long-wavelength result. These indicate that local field effects play a significant role. However, both correspond to the same onset, so the gap does not change.

D. Electron-hole effects: RPA vs BSE

Next, we show the optical dielectric functions for both polarizations comparing the RPA and BSE methods in Fig. 4. The curve labeled RPA is calculated following Eq. (4) or equivalently Eq. (7) but using P^0 instead of \bar{P} (it still includes e - h coupling by using \hat{W}), and the curve labeled BSE includes electron-hole coupling via Eq. (7). We can see that the BSE completely changes $\epsilon_2(\omega)$. There is a large shift down to lower energies. Remarkably, several peaks in the lowest energy absorption are excitonic in nature because they lie well below

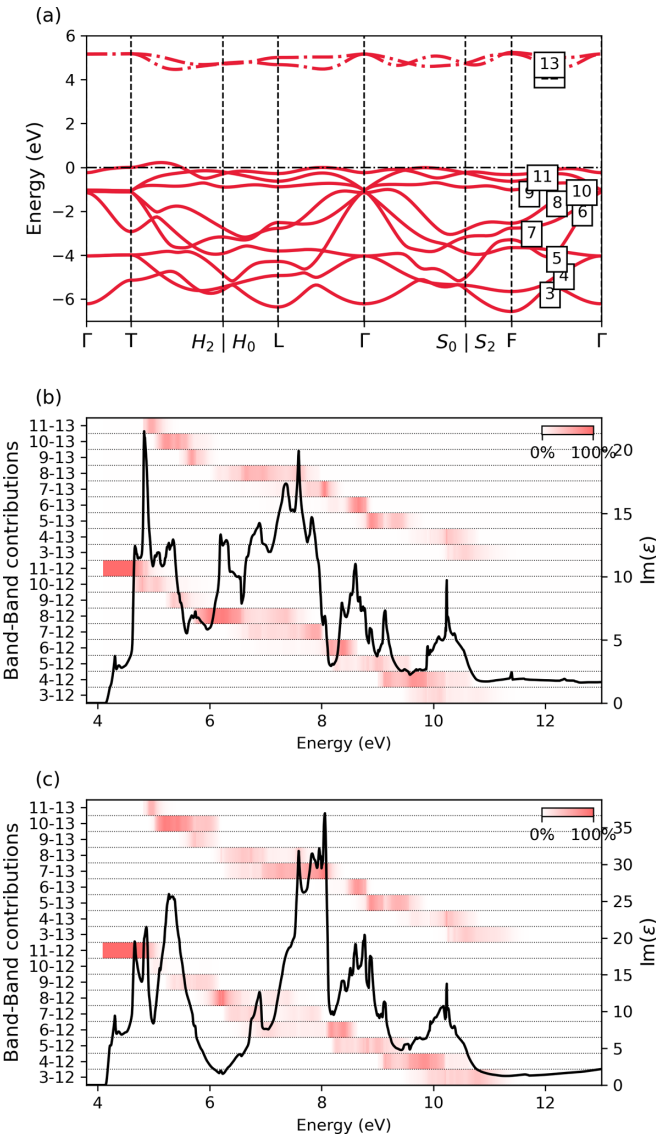


FIG. 2. Interband optical response function $\epsilon_2(\omega)$ calculated in long-wavelength approximation (no local field or excitonic effects). The partial contribution from a given band pair to the spectrum are shown as a color scale for each band pair: (a) band numbering (QSGW[†]), (b) $\mathbf{E} \parallel \mathbf{c}$, and (c) $\mathbf{E} \perp \mathbf{c}$.

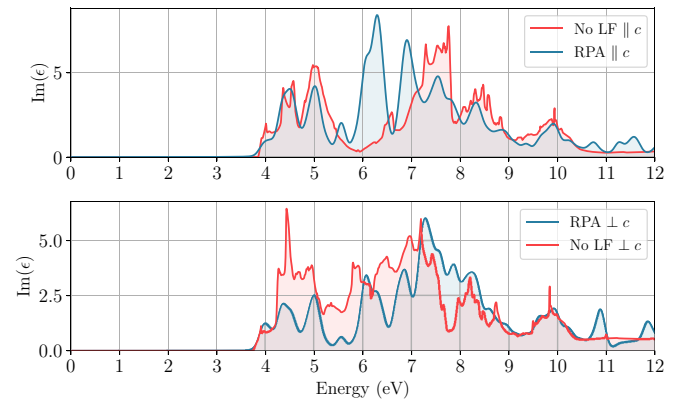


FIG. 3. Macroscopic dielectric function $\epsilon_2(\omega)$ for both polarizations comparing RPA [Eq. (4)] with the long-wavelength limit [Eq. (3)] without local field effects.

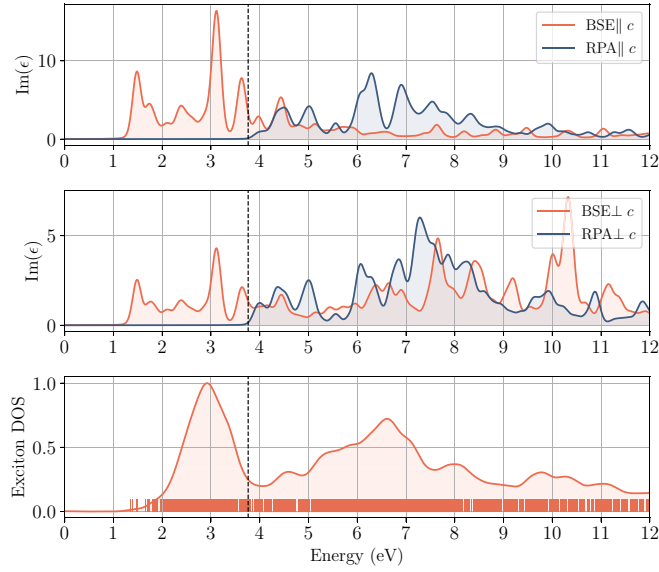


FIG. 4. Macroscopic optical dielectric function $\varepsilon_2(\omega)$ in RPA and BSE approximation both based on the QSGW band structure. Top to bottom, z polarization, in-plane polarization, and exciton density of states without optical matrix elements and exciton spectrum.

the quasiparticle fundamental gap. This indicates a very large exciton binding energy. This is related to the rather flat dispersion of the valence and conduction band which show several local maxima/minima in \mathbf{k} space. It is also indicative of the 2D character of the band structure in this layered compound. It is well known that lower dimensionality increases excitonic effects. The eigenvalues of the two-particle Hamiltonian or exciton level spectrum is shown in Fig. 1 in the rightmost panel. It shows that the lowest optical gap or excitonic gap, corresponding to the lowest exciton peak in Fig. 4, at ~ 1.5 eV is close to the LDA gap reported in Ref. [4] but still somewhat larger than our GGA band structure gap. A closer comparison with the exciton eigenvalues shows that the lowest exciton eigenvalue at 1.39 eV is dark and lies below the first exciton peak in ε_2 . We note that using W instead of \hat{W} would increase the quasiparticle gap but also increase the exciton binding energies and thus the final energy of the exciton binding energy may not be affected that much by omitting the ladder diagrams but it would increase the difference between quasiparticle and optical gap.

Because of this high exciton binding energy, we may consider this a Frenkel exciton and expect it also to be quite localized in real space. The density of exciton states is also shown in Fig. 4. So, this shows the density of the two-particle states including the electron-hole interaction but without weighing the intensity by optical matrix elements. It shows that the optical matrix elements are quite important in determining the actual optical spectrum. In other words, several of the two particle eigenvalues or exciton states are dark. For completeness, we also show the real part of the dielectric function in Fig. 5. It shows that the downward shift of the spectrum by BSE compared to RPA significantly affects the static $\varepsilon_1(\omega = 0)$, which is strongly enhanced.

Finally, in Appendix B we show that the BSE results using the RPA W instead of the ladder \hat{W} also shows strong excitons

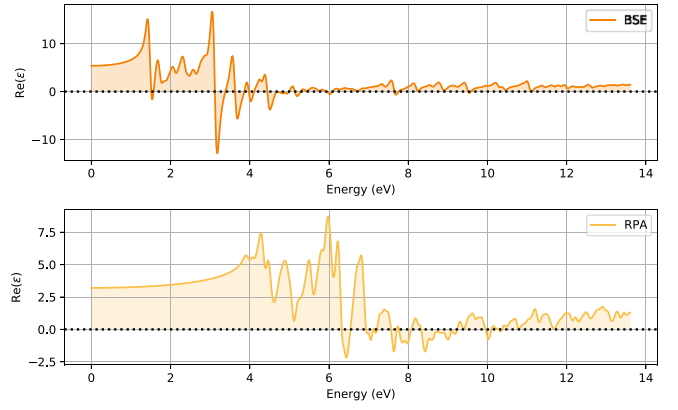


FIG. 5. Real part of $\varepsilon(\omega)$ in RPA and BSE for $\mathbf{E} \perp \mathbf{c}$.

with almost the same position of the lowest exciton peaks. However, in that case the difference between the fundamental gap of QSGW and the exciton or optical gap is even larger because the exciton binding energy increases with the larger W .

E. Further analysis of BSE

To gain further insight into the contributions of different bands to the excitons, we performed separate calculations in which we restrict the number of band pairs included in the basis set of the BSE calculation. This analysis is shown in Fig. 6. The first two sets of spectra from top to bottom focus on the contributions of the two Co- $d-e_g$ conduction bands while keeping all nine valence bands, derived from the six O- $2p$ and three Co- $d-t_{2g}$ bands. The thin line and gray filled curve shows the RPA $\varepsilon_2(\omega)$ in all cases. The second spectrum from the top shows the difference between the BSE including only the lowest conduction band c_1 and the RPA, or $\varepsilon_2^{\text{BSE}}(c_1, v_1 - v_9) - \varepsilon_2^{\text{RPA}}$. In the figure we label this as $\mathcal{I}_{1,\infty}$. The top curve shows the difference due to adding the second conduction band c_2 , so the $\varepsilon_2^{\text{BSE}}(c_1 - c_2, v_1 - v_9) - \varepsilon_2^{\text{BSE}}(c_1, v_1 - v_9)$. In the figure, this is labeled as $\mathcal{I}_{2,\infty}$. In the first step, one can see that spectral weight is pulled away from the RPA mostly from the region above 6 eV, which from our previous band to band analysis corresponds to interband transitions from the lower O- $2p$ related bands to the e_g bands. One can see that adding the second conduction band further shifts the lowest exciton peak down and increases its intensity, so both conduction bands contribute to the lowest energy exciton. The excitons near 3.5 eV also are shifted down to lower energy but stay above 3.0 eV and additional weight is pulled from the lower peaks above the CBM to the exciton region.

The next spectra from 3 and onward show the effect of adding valence bands one by one while keeping both conduction bands. Thus spectrum 3 from the top shows $\varepsilon_2^{\text{BSE}}(c_1 - c_2, v_1) - \varepsilon_2^{\text{RPA}}(\mathcal{I}_{\infty,1})$. Note that we count valence bands from top to bottom. Spectrum 4 shows $\varepsilon_2^{\text{BSE}}(c_1 - c_2, v_1 - v_2) - \varepsilon_2^{\text{BSE}}(c_1 - c_2, v_1)$, and so on. These spectra show that the lowest excitons are primarily pulling oscillator strengths from the first peaks above the gap in the RPA spectrum. The second valence band still shifts these down to lower energy and enhances their intensity. But adding more valence bands to the calculation no longer changes this spectrum, so the change in

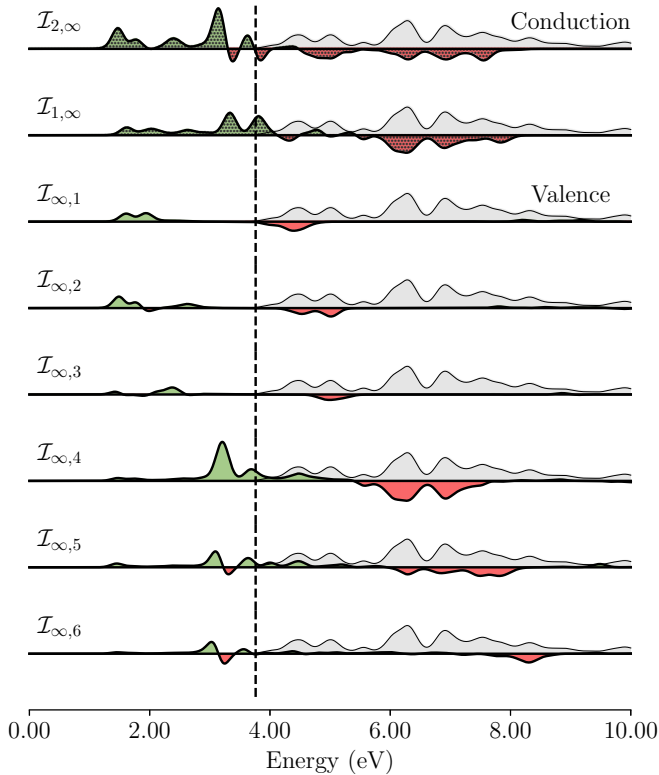


FIG. 6. Contributions to the BSE optical absorption from different bands. The gray filled spectrum is the RPA reference spectrum. $\mathcal{I}_{1,\infty}$ shows the difference between BSE, while including all valence bands but only the first conduction band, with RPA, $\mathcal{I}_{2,\infty}$ shows the difference between BSE including conduction bands 1,2 with only conduction band 1. $\mathcal{I}_{\infty,1}$ means all conduction bands included but only the top valence band in BSE relative to RPA, $\mathcal{I}_{\infty,2}$ means the difference between including valence bands 1,2 vs only 1 while keeping all conduction bands.

this region goes to zero. The exciton peak at about 2 eV comes in when we add the third valence band and pulls spectral weight primarily from the second RPA peak above the VBM. Finally, the peak at 3.5 eV is seen to appear only when we add valence band v_4 and pulls weight from the peaks above 6 eV in RPA. Further smaller changes occur in this exciton peaks when adding deeper valence bands, further shifting the peak downward and pulling spectral weight from higher and higher peaks in the RPA, which correspond to contributions from deeper valence bands with more and more O-2p character.

Next, we analyze which band pairs and \mathbf{k} points contribute to the $\varepsilon_2(\omega)$ exciton spectrum integrated over narrow energy ranges near the peaks of the exciton spectrum. We divide the BSE exciton region in separate intervals [1.26 – 1.6], [1.6 – 1.9], [1.9 – 2.21], [2.21 – 2.76], corresponding each to a separate peak in the optical spectrum. As an example, Fig. 7 shows which band state (n, \mathbf{k}) contribute to the exciton eigenvalues in the range 1.6–1.9 eV. We obtain this figure by using the eigenvectors $|A_{n,\mathbf{k}}^\lambda|^2$ as a weight at each \mathbf{k} and band n where λ indicates the exciton eigenvalue and then including all eigenvalues in the given energy range. This is then visualized as the size of the circles on the band structure. We can see that the top three valence bands and lowest two

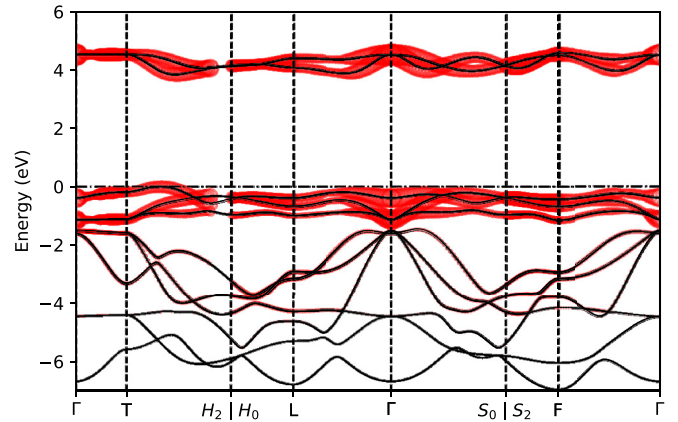


FIG. 7. Band contributions to the excitons in the range 1.6–1.9 eV.

conduction bands dominate the band content of these excitons. There is a somewhat smaller contribution from deeper valence bands. In terms of \mathbf{k} distribution, the contributions are almost uniformly spread over \mathbf{k} space. Similar conclusions hold if we examine the exciton band analysis for the other energy ranges. This is a clear indication that the excitons in this entire range are very broadly spread in \mathbf{k} space and consequently must be strongly localized in real space. We may thus call these excitons Frenkel excitons. In contrast, if we make such a plot for LiF, we see that the exciton peak is closely related to the valence band maximum and conduction band minimum near Γ and indicates a more delocalized Wannier-type exciton (shown in Appendix C).

F. Comparison with experiment

Unfortunately, at present no polarization dependent optical data are available for single crystals or well oriented films. The excitonic part of the BSE spectrum below the gap for $\mathbf{E} \perp \mathbf{c}$ shows several peaks between 1.3 and 3.8 eV, which is the value of the quasiparticle gap, with the strongest peaks at 1.5 and 3.2 eV. A main conclusion of our calculations is that the optical absorption gap should be significantly smaller than the single-particle gap. We now attempt to compare these with the various features in absorption reported by experimental studies.

Optical absorption involving the Co- d bands was first reported by Kushida and Kuriyama in sol-gel grown LiCoO₂ films [41,42]. They assigned an absorption peak around 2.1 eV to the transition between filled t_{2g} to empty e_g bands and a higher transition around 5 eV to Co- t_{2g} to Co-4s, mainly based on the Aydinol *et al.*'s [6] band structure calculations although they remark the calculations place the latter transitions at 7 eV. They also noticed a weaker absorption feature around 0.8 eV, which they claim cannot be defect associated but is rather related to “electronic structure near the e_g conduction band edge.” It is not clear what that means. They noticed this broad 2.1 eV peak becomes sharper in disordered spinel-like LiCoO₂ and shifts to 2.9 eV. They also compare it with a 2.3 eV gap in rocksalt CoO and associate the shift to lower gap with less strong covalent Co- d - e_g to O-2p interaction due to the larger Co-O distance.

TABLE II. Overview of band gap related optical features in theory and experiment.

	E_g (eV)	Ref.	Comment
Theory	1.2	[4]	LDA
	0.867	this work	GGA
	4.125	this work	E_g^{qp} QSGW
	3.762	this work	E_g^{qp} QSG \hat{W}
	1.5	this work	E_g^{opt} lowest bright exciton peak
Experiment	2.1	[41]	absorption peak t_{2g} - e_g
	1.43	[44]	differentiation of absorption
	2.5	[45]	Tauc plot
	2.3	[46]	Tauc plot
	1.7	[43]	optical absorption
	> 3.0	[5]	XPS/BIS

Optical absorption of Li_xCoO_2 as function of x was reported by Liu *et al.* [43], who associate the 1.7 eV peak which they find to be present only in Li_xCoO_2 with $x < 0.72$ to transitions from a peak in the filled t_{2g} to empty t_{2g} states within the same band and a peak at 3.08 eV to t_{2g} - e_g transitions and higher peaks around 4.55 and 5.76 eV to transitions from lower more O-2p hybridized valence bands to the e_g conduction band.

Ghosh *et al.* [44] determine the gap at about 1.43 eV by differentiating the absorption spectrum. They claim this is in good agreement with the earlier band calculations by Czyżyk *et al.* [4] although that paper mentions a calculated gap of only 1.2 eV. Instead, we identify this feature and the closely associated peak at 1.7 eV with our lowest excitonic peak at 1.5 eV. The 3.0 eV feature seen by Liu *et al.* [43] could be compared with our exciton peak at 3.2 eV. Lower energy features at 0.88 and 0.65 eV in Ghosh *et al.* were there associated with defects but are similar to those observed by Kushida *et al.* in other phases of LiCoO_2 only. On the other hand, our analysis of the band-to-band origin of peaks in absorption shows that transitions from the highest valence band to higher conduction bands, beyond the e_g Co bands, related to Co-4s or Li occur at much higher energy and features near 5 eV in optical absorption must rather be due to transitions from deeper valence bands to the same Co- e_g conduction band.

Balakrishnan *et al.* [45] used Tauc plots to extrapolate a gap between 2.5 and 3.24 eV depending on annealing temperature of their sol-gel grown films. The largest gap value here corresponded to the highest annealing temperature. These data also show a lower peak in optical absorption between 2.5 and 3.0 eV. Rao [46] also used Tauc plots (on pulsed laser deposited films) but places the onset of absorption at about 2.3–2.4 eV. The Tauc method consists of plotting the absorption coefficient squared and then extrapolating a linear slope fitted to the low energy region. However, we caution that the Tauc plot analysis to determine the gap is based on the expectation of a square-root behavior of the joint density of states just above the threshold and is expected to be valid only for direct gap semiconductors in the absence of excitons, for example at high enough temperature that the excitons become

dissociated. Our calculations show that the lowest peaks in optical absorption are excitonic in nature with high exciton binding energies and do not support the validity of a Tauc model analysis.

As for the various experimental observations as function of temperature, we note that at higher temperature, one may expect interdiffusion of Li inside the CoO_2 layer and formation of disordered rocksalt or spinel type phases [40]. These could have significantly different optical absorption properties because they have a different electronic structure. These structures would lack the 2D like strong binding energy and would be characterized by disorder in the Li locations which may also have strongly correlated aspects by the deviations from the ideal octahedral splitting of the Co d bands into filled t_{2g} and empty e_g bands.

Support for our assertion that the quasiparticle gap is significantly larger than the optical absorption gap is provided by the Bremsstrahlung isochromat spectroscopy (BIS) or inverse photoemission and x-ray photoemission spectroscopy (XPS) by van Elp *et al.* [5]. Although their theoretical analysis in terms of a cluster model places the experimental gap at 2.7 ± 0.3 eV, the BIS-XPS actual data in their figures are consistent with a quasiparticle gap larger than 3 eV.

An overview of the different experimental and theoretical band gap and associated optical features is given in Table II.

Thus, our lowest exciton peak at 1.5 eV and an additional peak at about 3.2 eV may be considered to be consistent with experimental observations at the onset of optical absorption. However, the sharp nature of the excitonic peaks predicted by the BSE is apparently not seen in the experiment. This may be because of the finite temperature broadening, electron-phonon coupling, and so on, which are not yet taken into account by our present calculation, which only used an ad-hoc broadening parameter in the BSE spectra. We stress that the present BSE calculations provide a radically different interpretation of the optical absorption onset than early LDA band structure interpretations.

Clearly, additional experimental work on single crystal samples including polarization dependence would be useful to further explore the nature of the optical absorption onset and confirm our conclusion of its excitonic nature.

IV. CONCLUSIONS

The main conclusion of this work is that the onset of optical absorption in LiCoO_2 is excitonic in nature and shows a significant binding energy with respect to the independent particle band gap as obtained in a GW approximation and which would correspond to the difference between BIS and XPS experiments. More precisely we find that the QSGW gaps of 4.15 eV is much larger than the GGA gap of 0.87 eV. The electron hole interactions increase the screening of W and lower the QSGW gap by about 11% but the quasiparticle gap is then still at about 3.76 eV and cannot explain the lower onsets of absorption. However, the excitonic BSE spectrum has an onset which is shifted back down well below the quasiparticle gap and shows a lowest excitonic peak near 1.5 eV which agrees with the experimentally found absorption onset at 1.4 eV and lowest absorption peaks near 2 eV. A second excitonic peak at about 3.3 eV is also hinted at in some

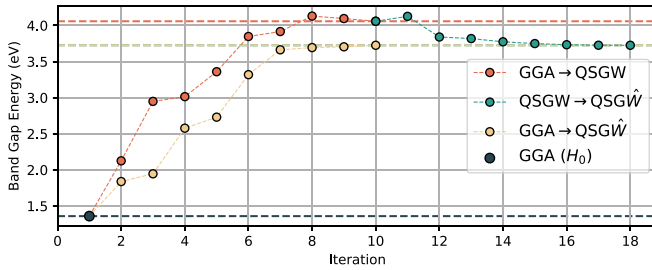


FIG. 8. Convergence of the gap as function of iteration number in QSGW and QSGW \hat{W} .

experimental results. Nonetheless significant questions about the detailed interpretation of the experiments remain because of possible complications with disordered phases of LiCoO₂, variation in Li content, and so on.

ACKNOWLEDGMENTS

The work at CWRU (S.K.R. and W.R.L.L.) was supported by the Air Force Office of Scientific Research under Grant No. FA9550-18-1-0030. The calculations made use of the High Performance Computing Resource in the Core Facility for Advanced Research Computing at Case Western Reserve University. B.C., M.G., D.P., and M.v.S. are grateful for support from the Engineering and Physical Sciences Research Council (EPSRC), under Grant EP/M011631/1. M.v.S. and D.P. are supported by the National Renewable Energy Laboratory.

APPENDIX A: CONVERGENCE

Figure 8 shows the convergence of the gap in QSGW followed by several iterations in which ladder diagrams are included using \hat{W} compared with using the ladder diagrams from the start.

APPENDIX B: BSE WITH W VS \hat{W}

Figure 9 shows that $\epsilon_2(\omega)$ calculated with W in the RPA is similar but not identical to the one calculated with \hat{W} includ-

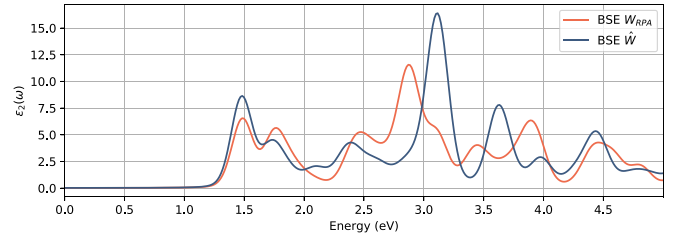


FIG. 9. Comparison of imaginary part of the dielectric function $\epsilon_2(\omega)$ (for $\mathbf{E} \parallel \mathbf{c}$) with W calculated in RPA and \hat{W} calculated including ladder diagrams both in the underlying band structure and BSE. This is because the larger W in the RPA increases the fundamental gap of QSGW but also increases the exciton binding energies in a proportional manner.

APPENDIX C: LiF

To distinguish the Frenkel excitons found in this paper for LiCoO₂ which have a very delocalized origin in band states in \mathbf{k} space, we show here in Fig. 10 the corresponding figure for LiF. The good agreement with other calculations, for example using the exciting code [47,48], for this \mathbf{k} -space origin of the exciton in LiF, which has Wannier exciton character also serves to demonstrate the validity of our methodology.

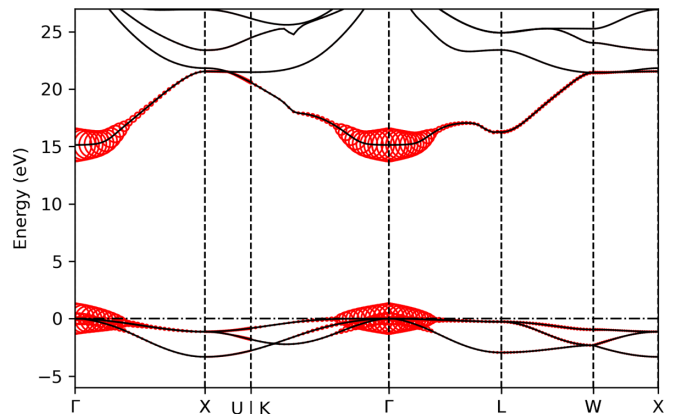


FIG. 10. Exciton projected band structure for LiF.

- [1] K. Mizushima, P. Jones, P. Wiseman, and J. Goodenough, Li_xCoO₂ ($0 < x < -1$): A new cathode material for batteries of high energy density, *Mater. Res. Bull.* **15**, 783 (1980).
- [2] K. Miyoshi, K. Manami, R. Sasai, S. Nishigori, and J. Takeuchi, Electronic states realized by the interplay between Li diffusion and Co³⁺/Co⁴⁺ charge ordering in Li_xCoO₂, *Phys. Rev. B* **98**, 195106 (2018).
- [3] K. Iwaya, T. Ogawa, T. Minato, K. Miyoshi, J. Takeuchi, A. Kuwabara, H. Moriwake, Y. Kim, and T. Hitosugi, Impact of Lithium-Ion Ordering on Surface Electronic States of Li_xCoO₂, *Phys. Rev. Lett.* **111**, 126104 (2013).
- [4] M. T. Czyżyk, R. Potze, and G. A. Sawatzky, Band-theory description of high-energy spectroscopy and the electronic structure of LiCoO₂, *Phys. Rev. B* **46**, 3729 (1992).
- [5] J. van Elp, J. L. Wieland, H. Eskes, P. Kuiper, G. A. Sawatzky, F. M. F. de Groot, and T. S. Turner, Electronic structure of CoO, Li-doped CoO, and LiCoO₂, *Phys. Rev. B* **44**, 6090 (1991).
- [6] M. K. Aydinol, A. F. Kohan, G. Ceder, K. Cho, and J. Joannopoulos, *Ab initio* study of lithium intercalation in metal oxides and metal dichalcogenides, *Phys. Rev. B* **56**, 1354 (1997).
- [7] C. Wolverton and A. Zunger, First-Principles Prediction of Vacancy Order-Disorder and Intercalation Battery Voltages in Li_xCoO₂, *Phys. Rev. Lett.* **81**, 606 (1998).
- [8] C. A. Marianetti, G. Kotliar, and G. Ceder, A first-order Mott transition in Li_xCoO₂, *Nat. Mater.* **3**, 627 (2004).
- [9] L. Seguin, G. Amatucci, M. Anne, Y. Chabre, P. Strobel, J. Tarascon, and G. Vaughan, Structural study of NiO₂ and CoO₂ as end members of the lithiated compounds by in situ high resolution x-ray powder diffraction, *J. Power Sources* **81-82**, 604 (1999).

- [10] M. I. Aroyo, D. Orobengoa, G. de la Flor, E. S. Tasci, J. M. Perez-Mato, and H. Wondratschek, Brillouin-zone database on the Bilbao Crystallographic Server, *Acta Crystallogr. Sect. A* **70**, 126 (2014).
- [11] Y. Hinuma, G. Pizzi, Y. Kumagai, F. Oba, and I. Tanaka, Band structure diagram paths based on crystallography, *Comput. Mater. Sci.* **128**, 140 (2017).
- [12] T. Kotani and M. van Schilfhaarde, Fusion of the LAPW and LMTO methods: The augmented plane wave plus muffin-tin orbital method, *Phys. Rev. B* **81**, 125117 (2010).
- [13] M. Methfessel, M. van Schilfhaarde, and R. A. Casali, A Full-potential LMTO method based on smooth Hankel functions, in *Electronic Structure and Physical Properties of Solids. The Use of the LMTO Method*, Lecture Notes in Physics, Vol. 535, edited by H. Dreyssé (Springer, Berlin, 2000), p. 114.
- [14] D. Pashov, S. Acharya, W. R. L. Lambrecht, J. Jackson, K. D. Belashchenko, A. Chantis, F. Jamet, and M. van Schilfhaarde, Questaal: A package of electronic structure methods based on the linear muffin-tin orbital technique, *Comput. Phys. Commun.* **249**, 107065 (2020).
- [15] See <https://www.questaal.org>.
- [16] J. P. Perdew, K. Burke, and M. Ernzerhof, Generalized Gradient Approximation Made Simple, *Phys. Rev. Lett.* **77**, 3865 (1996).
- [17] T. Kotani, M. van Schilfhaarde, and S. V. Faleev, Quasiparticle self-consistent GW method: A basis for the independent-particle approximation, *Phys. Rev. B* **76**, 165106 (2007).
- [18] B. Cunningham, M. Grüning, P. Azarhoosh, D. Pashov, and M. van Schilfhaarde, Effect of ladder diagrams on optical absorption spectra in a quasiparticle self-consistent GW framework, *Phys. Rev. Materials* **2**, 034603 (2018).
- [19] B. Cunningham, M. Gruening, D. Pashov, and M. van Schilfhaarde, QSGW: Quasiparticle self-consistent GW with ladder diagrams in W, [arXiv:2106.05759](https://arxiv.org/abs/2106.05759).
- [20] M. Shishkin, M. Marsman, and G. Kresse, Accurate Quasiparticle Spectra from Self-Consistent GW Calculations with Vertex Corrections, *Phys. Rev. Lett.* **99**, 246403 (2007).
- [21] W. Chen and A. Pasquarello, Accurate band gaps of extended systems via efficient vertex corrections in GW, *Phys. Rev. B* **92**, 041115(R) (2015).
- [22] A. Tal, W. Chen, and A. Pasquarello, Vertex function compliant with the Ward identity for quasiparticle self-consistent calculations beyond GW, *Phys. Rev. B* **103**, L161104 (2021).
- [23] A. Marini and R. Del Sole, Dynamical Excitonic Effects in Metals and Semiconductors, *Phys. Rev. Lett.* **91**, 176402 (2003).
- [24] A. Grüneis, G. Kresse, Y. Hinuma, and F. Oba, Ionization Potentials of Solids: The Importance of Vertex Corrections, *Phys. Rev. Lett.* **112**, 096401 (2014).
- [25] E. Maggio and G. Kresse, GW vertex corrected calculations for molecular systems, *J. Chem. Theory Comput.* **13**, 4765 (2017).
- [26] A. L. Kutepov, Electronic structure of Na, K, Si, and LiF from self-consistent solution of Hedin's equations including vertex corrections, *Phys. Rev. B* **94**, 155101 (2016).
- [27] A. L. Kutepov, Self-consistent solution of Hedin's equations: Semiconductors and insulators, *Phys. Rev. B* **95**, 195120 (2017).
- [28] Z. H. Levine and D. C. Allan, Linear Optical Response in Silicon and Germanium Including Self-Energy Effects, *Phys. Rev. Lett.* **63**, 1719 (1989).
- [29] W. Hanke, Dielectric theory of elementary excitations in crystals, *Adv. Phys.* **27**, 287 (1978).
- [30] G. Onida, L. Reining, and A. Rubio, Electronic excitations: density-functional versus many-body Green's-function approaches, *Rev. Mod. Phys.* **74**, 601 (2002).
- [31] P.-F. Loos, B. Pradines, A. Scemama, E. Giner, and J. Toulouse, Density-based basis-set incompleteness correction for GW methods, *J. Chem. Theory Comput.* **16**, 1018 (2020).
- [32] J. A. Berger, L. Reining, and F. Sottile, *Ab initio* calculations of electronic excitations: Collapsing spectral sums, *Phys. Rev. B* **82**, 041103(R) (2010).
- [33] M. Betzinger, C. Friedrich, A. Görling, and S. Blügel, Precise all-electron dynamical response functions: Application to COHSEX and the RPA correlation energy, *Phys. Rev. B* **92**, 245101 (2015).
- [34] M. van Schilfhaarde, T. Kotani, and S. V. Faleev, Adequacy of approximations in GW theory, *Phys. Rev. B* **74**, 245125 (2006).
- [35] M. Betzinger, C. Friedrich, and S. Blügel, Precise response functions in all-electron methods: Generalization to nonspherical perturbations and application to NiO, *Phys. Rev. B* **88**, 075130 (2013).
- [36] C. Friedrich, M. C. Müller, and S. Blügel, Erratum: Band convergence and linearization error correction of all-electron GW calculations: The extreme case of zinc oxide [Phys. Rev. B **83**, 081101(R) (2011)], *Phys. Rev. B* **84**, 039906(E) (2011).
- [37] H. Jiang and P. Blaha, GW with linearized augmented plane waves extended by high-energy local orbitals, *Phys. Rev. B* **93**, 115203 (2016).
- [38] T. Sander, E. Maggio, and G. Kresse, Beyond the Tamm-Dancoff approximation for extended systems using exact diagonalization, *Phys. Rev. B* **92**, 045209 (2015).
- [39] See, <https://tools.materialscloud.org/seekpath/>.
- [40] H. Volkova, K. Pachuta, K. Crowley, S. K. Radha, E. Pentzer, X. P. A. Gao, W. R. L. Lambrecht, A. Sehirlioglu, and M.-H. Berger, Electron microscopy and spectroscopic study of structural changes, electronic properties, and conductivity in annealed Li_xCoO₂, *Phys. Rev. Materials* **5**, 015401 (2021).
- [41] K. Kushida and K. Kuriyama, Optical absorption related to Co-3d bands in sol-gel grown LiCoO₂ films, *Solid State Commun.* **118**, 615 (2001).
- [42] K. Kushida and K. Kuriyama, Narrowing of the Co-3d band related to the order-disorder phase transition in LiCoO₂, *Solid State Commun.* **123**, 349 (2002).
- [43] H. L. Liu, T. Y. Ou-Yang, H. H. Tsai, P. A. Lin, H. T. Jeng, G. J. Shu, and F. C. Chou, Electronic structure and lattice dynamics of Li_xCoO₂ single crystals, *New J. Phys.* **17**, 103004 (2015).
- [44] P. Ghosh, S. Mahanty, M. Raja, R. Basu, and H. Maiti, Structure and optical absorption of combustion-synthesized nanocrystalline LiCoO₂, *J. Mater. Res.* **22**, 1162 (2007).
- [45] T. Balakrishnan, N. Sankarasubramanian, A. Kavitha, and A. Kathalingam, Studies on structural, optical, electrical and morphological properties of LiCoO₂ thin films prepared by sol-gel method, *Mater. Res. Innovations* **23**, 216 (2019).
- [46] M. C. Rao and O. M. Hussain, Optical and electrical properties of laser ablated amorphous LiCoO₂ thin film cathodes, *IOP Conf. Ser.: Mater. Sci. Eng.* **2**, 012037 (2009).
- [47] See <http://exciting.wikidot.com/oxygen-exciton-visualization;10.17172/NOMAD/2020.07.14-2>.
- [48] C. Vorwerk, B. Aurich, C. Cocchi, and C. Draxl, Bethe-Salpeter equation for absorption and scattering spectroscopy: Implementation in the exciting code, *Electron. Struct.* **1**, 037001 (2019).